Potential of glassy carbon and silicon carbide photonic structures as electromagnetic radiation shields for atmospheric re-entry

Nikolay Komarevskiy[1], Valery Shklover[1], Leonid Braginsky[1], Christian Hafner[1], and John Lawson[2]

[1]*Swiss Federal Institute of Technology (ETH) Zürich, 8092 Zürich, Switzerland*
[2]*MS-234-1, NASA Ames Research Center, Moffett Field, 94035 California, USA*

n.komarevskiy@ifh.ee.ethz.ch

Abstract: During high-velocity atmospheric entries, space vehicles can be exposed to strong electromagnetic radiation from ionized gas in the shock layer. Glassy carbon (GC) and silicon carbide (SiC) are candidate thermal protection materials due to their high melting point and also their good thermal and mechanical properties. Based on data from shock tube experiments, a significant fraction of radiation at hypersonic entry conditions is in the frequency range from 215 to 415 THz. We propose and analyze SiC and GC photonic structures to increase the reflection of radiation in that range. For this purpose, we performed numerical optimizations of various structures using an evolutionary strategy. Among the considered structures are layered, porous, woodpile, inverse opal and guided-mode resonance structures. In order to estimate the impact of fabrication inaccuracies, the sensitivity of the reflectivity to structural imperfections is analyzed. We estimate that the reflectivity of GC photonic structures is limited to 38% in the aforementioned range, due to material absorption. However, GC material can be effective for photonic reflection of individual, strong spectral line. SiC on the other hand can be used to design a good reflector for the entire frequency range.

OCIS codes: (050.5298) Photonic crystals; (350.4600) Optical engineering

References and links

1. J. Joannopoulos, S. Johnson, J. Winn, and R. Meade, *Photonic crystals: molding the flow of light* (Princeton Univ Pr, 2008).
2. V. Shklover, L. Braginsky, G. Witz, M. Mishrikey, and C. Hafner, "High-Temperature Photonic Structures. Thermal Barrier Coatings, Infrared Sources and Other Applications," Journal of Computational and Theoretical Nanoscience **5**, 862 (2008).
3. J. Grinstead, M. Wilder, J. Olejniczak, D. Bogdanoff, G. Allen, K. Dang, and M. Forrest, "Shock-heated Air Radiation Measurements at Lunar Return Conditions," AIAA Paper **1244**, 2008 (2008).
4. C. Park, "Stagnation-region heating environment of the galileo probe," Journal of thermophysics and heat transfer **23**, 417–424 (2009).
5. N. Komarevskiy, L. Braginsky, V. Shklover, C. Hafner, and J. Lawson, "Fast numerical methods for the design of layered photonic structures with rough interfaces," Optics Express **19**, 5489–5499 (2011).
6. N. Komarevskiy, V. Shklover, L. Braginsky, C. Hafner, O. Fabrichnaya, S. White, and J. Lawson, "Design of reflective, photonic shields for atmospheric reentry," Journal of Electromagnetic Analysis and Applications **3**, 228–237 (2011).

7. A. Brandis, C. Johnston, B. Cruden, D. Prabhu, and D. Bose, "Uncertainty analysis of neqair and hara predictions of air radiation measurements obtained in the east facility," in "42nd AIAA Thermophysics Conference," (American Institute of Aeronautics & Astronautics (AIAA), 2011).
8. L. Li, "Formulation and comparison of two recursive matrix algorithms for modeling layered diffraction gratings," Journal of the optical society of America **13**, 1024–1035 (1996).
9. D. Whittaker and I. Culshaw, "Scattering-matrix treatment of patterned multilayer photonic structures," Physical Review B **60**, 2610–2618 (1999).
10. J. Fröhlich, "Evolutionary optimization for computational electromagnetics," Ph.D. thesis, ETH Zurich, IFH Laboratory (1997).
11. [Online]. Available: http://www.sopra-sa.com/
12. E. D. Palik, *Handbook of Optical Constants of Solids* (Academic Press, 1998).
13. M. Williams and E. Arakawa, "Optical properties of glassy carbon from 0 to 82 ev," Journal of Applied Physics **43**, 3460–3463 (1972).
14. J. Shor, I. Grimberg, B. Weiss, and A. Kurtz, "Direct observation of porous sic formed by anodization in hf," Applied physics letters **62**, 2836–2838 (1993).
15. A. Zakhidov, R. Baughman, Z. Iqbal, C. Cui, I. Khayrullin, S. Dantas, J. Marti, and V. Ralchenko, "Carbon structures with three-dimensional periodicity at optical wavelengths," Science **282**, 897 (1998).
16. S. Wang and R. Magnusson, "Theory and applications of guided-mode resonance filters," Applied optics **32**, 2606–2613 (1993).
17. M. Gale, K. Knop, and R. Morf, "Zero-order diffractive microstructures for security applications," in "Proceedings of SPIE," , vol. 1210 (1990), vol. 1210, p. 83.
18. Z. Liu, S. Tibuleac, D. Shin, P. Young, and R. Magnusson, "High-efficiency guided-mode resonance filter," Optics letters **23**, 1556–1558 (1998).
19. S. Tikhodeev, A. Yablonskii, E. Muljarov, N. Gippius, and T. Ishihara, "Quasiguided modes and optical properties of photonic crystal slabs," Physical Review B **66**, 45102 (2002).
20. L. Braginsky and V. Shklover, "Light propagation in an imperfect photonic crystal," Physical Review B **73**, 85107 (2006).

1. Introduction

Practical applications for photonic crystals (PhCs) are vast [1, 2]. The optical response of PhCs can be effectively controlled via structural design. An interesting, but one yet to be practically realized, application of PhCs is as radiation shields for atmospheric re-entry of space vehicles. Electromagnetic radiation from ionized gas in the shock layer can constitute up to 30-50% [3] of the overall heat flux for lunar return trajectories, albeit for relatively short times. For Jupiter entries, on the other hand, most of the heating is radiative [4]. Therefore, in addition to protection against convective heating, a reentry thermal protection systems (TPS) should also be designed for radiation shielding. Ideally, the design should be tuned to the radiative spectra of a specific planet as well as to the specific entry conditions.

The easiest way to design radiation shields for atmospheric re-entry is with layered media [5]. Provided the two constituent materials possess a sufficient dielectric contrast and low absorption, broadband radiation shields with high omnidirectional reflection can be designed [6]. However, applications such as atmospheric re-entry impose many additional constraints on the material properties (thermal, mechanical, etc.). Therefore, finding a suitable pair of materials can be very demanding.

Currently, TPS for the most demanding atmospheric re-entries are made of highly porous carbon based materials. These materials, for example, PICA (phenolic-impregnated carbon ablators), possess many of the required thermal and mechanical properties. However, these materials are strong absorbers of radiation and therefore currently offer no protection at all from radiative heating. On the other hand, if these materials could be structured in such way that high reflection is obtained, radiative heating of the vehicle during re-entry could be reduced. In this paper we analyze the potential of glassy carbon and silicon carbide as radiation shields for Earth atmospheric re-entry.

The structure of the paper is as follows. In Sec. 2 we analyze the radiative spectra obtained for Earth re-entry conditions and define the optimization goal. In Sec. 3 optical properties of

SiC and GC are discussed and optimizations of one-dimensional structures are performed. The potential of GC as a single frequency reflector is considered in Sec. 4. In Sec. 5 optimization of SiC guided-mode resonance structures is performed. An SiC woodpile structures and porous-reflectors are optimized in Sec. 6. Finally, in Sec. 7 we analyze the sensitivity of the reflectivity to geometrical imperfections.

2. Problem definition

During an Earth atmospheric re-entry, a space vehicle can be exposed to strong radiation from ionized shocked gases whose intensity will depend on the entry velocity. Figure 1(a)-(c) presents spectra obtained for Earth re-entry relevant conditions at the EAST (Electric Arc Shock Tube) facility [7]. The spectra contains many sharp peaks corresponding to emission from various atomic and molecular species of the gas. Analyzing the broad radiation spectra, we select the *optimization range* **B**=215-415 THz or 720-1400 nm which captures 51% of the overall measured radiation. Outside of this range, approximately 26% of the radiation lies in three narrow regions near $f_1 = 1718$, $f_2 = 2008$ and $f_3 = 2300$ THz and the remaining 23% is in the rest of the spectrum.

Because of the sharpness of the peaks in the **B** range (see Fig. 1) and the inevitable uncertainty in the intensity values, it is reasonable to smooth the experimental curve. We do this using a Gaussian window function. The resulting smoothed curve u_ν is shown in Fig. 1(a). The area under the experimental and smoothed curve remain the same.

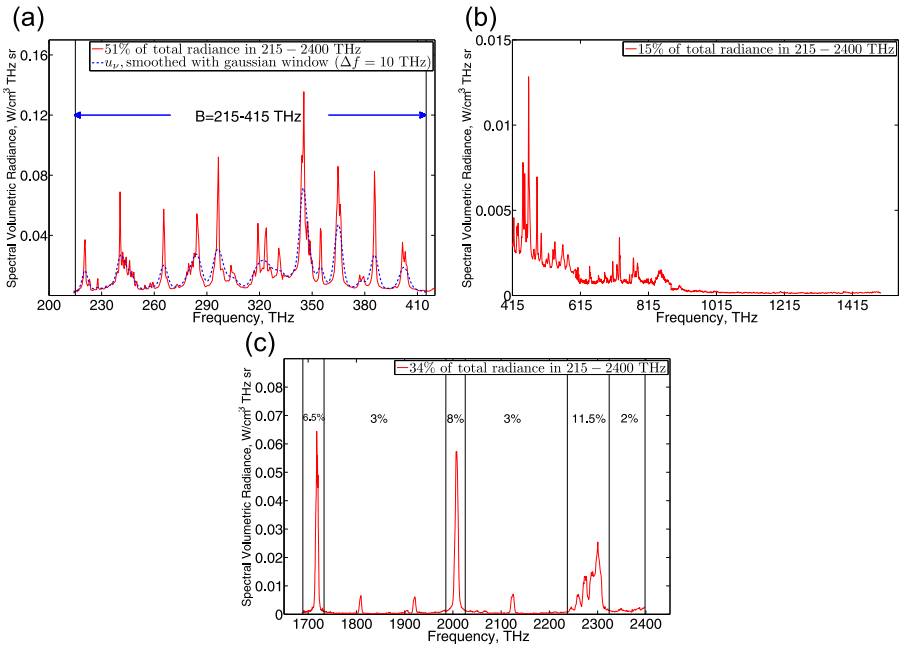

Fig. 1. (a)-(c) Experimental data of spectral radiation distribution, obtained at atmospheric re-entry relevant conditions [7] (a) red - experimental radiative spectrum in the range **B**=215-415 THz, blue dashed curve - spectrum smoothed with Gaussian window function of full width $\Delta f = 10$ THz.

In principle, radiation impinges on the surface of the vehicle at all angles θ. However, shock gases not only emit radiation, but also absorb it. Therefore, the radiation intensity u_ν

that reaches the surface should be sharply peaked around normal incidence [1]. Because of this, we consider only normally incident light, with the smoothed radiation spectra u_ν, shown in Fig. 1(a).

The goal is to design a radiation shield that maximizes the total reflection of normally incident *unpolarized* radiation u_ν. Therefore, the function to be maximized is:

$$\langle R_{u_\nu} \rangle = \frac{\int \mathrm{R}_\Sigma u_\nu d\nu}{\mathrm{u_{tot}}}, \ \mathrm{u_{tot}} = \int u_\nu d\nu, \tag{1}$$

where integration is performed over the **B** range, R_Σ is the total reflection of the incident unpolarized radiation:

$$\mathrm{R}_\Sigma = 0.5(\mathrm{R^s} + \mathrm{R^p}), \tag{2}$$

where $\mathrm{R^s}$ and $\mathrm{R^p}$ are the sum of reflection efficiencies for the s- and p-polarization, respectively:

$$\mathrm{R^{s,p}} = \mathrm{R_0^{s,p}} + \sum \mathrm{D_i^{s,p}}, \ \mathrm{i} = \pm 1, \pm 2, \ldots \tag{3}$$

here the summation is performed over the propagating diffraction orders in the upper air half space. Hereafter, we will refer to $\langle R_{u_\nu} \rangle$ as the "reflection".

For uniform radiation $u_\nu = 1$, the Expr. (1) reads:

$$\langle R \rangle = \frac{\int \mathrm{R}_\Sigma d\nu}{\Delta\nu}. \tag{4}$$

For calculations of the structures, considered in Sec. 3-5 we used the scattering matrix approach [8, 9]. CST Studio (Frequency Domain Solver) was used for calculations of the inverse opal structure, considered in Sec. 4 and of structures, considered in Sec. 6.

For numerical optimization, we used evolutionary strategy (ES) algorithms. Based on previous experience [10], ES is very powerful for real parameter optimization problems and outperforms genetic algorithm, particle swarm optimization, and other methods in most cases. We used an (*m*+*n*) ES with adaptive mutation for the optimization in the following example.

Here m is the initial number of parents and n is the number of children created in each generation. In the following calculations, $m = 6$ and $n = 7m$ were used.

3. One-dimensional silicon carbide and glassy carbon structures

Permittivity data for SiC and GC are shown in Fig. 2. SiC is optically transparent in the **B** range and almost non-dispersive with $\varepsilon \simeq 6.7$. Optical transparency of SiC implies that an ideal reflector can be designed, provided the photonic structure is sufficiently thick. It should also be noted that bulk SiC reflects c.a. 50% of the radiation in 1700-2400 THz, where the three strong radiation peaks are located. This effect is mostly due to high $\mathrm{Im}(\varepsilon)$ and partly due to negative $\mathrm{Re}(\varepsilon)$ in this frequency range. Permittivity data from [11] are used for SiC in all further calculations.

The one-dimensional SiC/air structure shows rapid convergence of $\langle R_{u_\nu} \rangle$ to unity as the number of layers increases, see Fig. 3(a). The reflectivity of an optimal monolayer is already rather high $\langle R_{u_\nu} \rangle = 53\%$. With three SiC layers, $\langle R_{u_\nu} \rangle = 97\%$ is achieved. Figure. 3(c) shows the reflection spectra of the optimal structure, containing four SiC layers. In practice such one-dimensional SiC/air structures can be realized approximately, for example, if the air layers are

[1] Directionality can be obtained from simulation sets that are calibrated against shock tube data

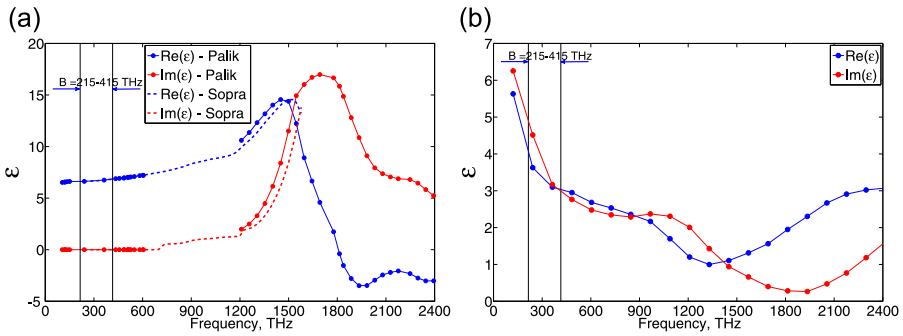

Fig. 2. Permittivity of (a) SiC taken from [11, 12] (b) GC taken from [13].

substituted with porous SiC layers. If the pore size $d << \lambda_{\min} = 720$ nm, then the porous SiC layers can be treated in calculations with the effective media approach. Fabrication of porous SiC with pore size $d = 10 - 30$ nm was reported in [14]. In Sec. 6, we will consider a porous-reflector, however with pore sizes $d \sim \lambda_{\min}$, where the effective medium theory does not hold.

In contrast to SiC, GC is very absorptive in the **B** range. The skin depth at $\lambda = 800$ nm is $\Delta_s = 170$ nm, $\Delta_s << \lambda$. This implies that radiation shields with high reflectivity are very difficult to design using GC. Also, small Δ_s implies, that the fraction of GC in the photonic structure should be much smaller than that of air. In other words GC should be used very sparingly.

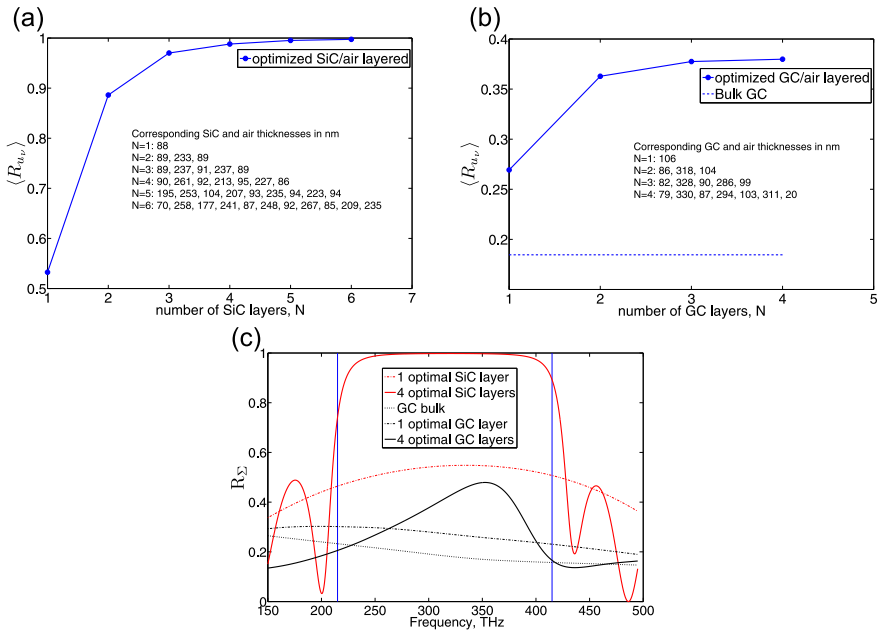

Fig. 3. 1D structures optimized with ES for reflection of radiation u_V (a) SiC/air (b) GC/air (c) reflection spectra of the structures.

In order to estimate the maximum attainable reflection (defined in Expr. (1)) with GC material, we can proceed with the following arguments. For any two-component system (GC/air in our case) the structure, which has the widest photonic band gap for the chosen direction of the

wave vector $\vec{k}$ is 1D-periodic [2]. Therefore, among all possible photonic structures, a 1D GC/air structure should maximize the reflection of normally incident light for both a single frequency or a frequency range **B**. The dependence of $\langle R_{u_v} \rangle$, as a function of the number of GC layers is shown in Fig. 3(b). As can be seen, already with two layers almost the maximum reflection with the value $\langle R_{u_v} \rangle \simeq 38\%$ is reached. While still relatively low, this value is more than 2X the bulk value of 18%. Figure 3(c) shows the reflection spectra of the optimal GC/air structure, containing four GC layers.

4. Glassy carbon structures as single frequency reflectors

As shown in the previous section, it is problematic to design a good broadband reflector with GC. However, rather high reflectivity can be achieved with GC for a single frequency. As an example, we optimized a periodic 1D GC/air structure for the reflection of the strongest line at $f = 345$ THz. The dependence of the reflection on the number of periods is shown in Fig. 4(a).

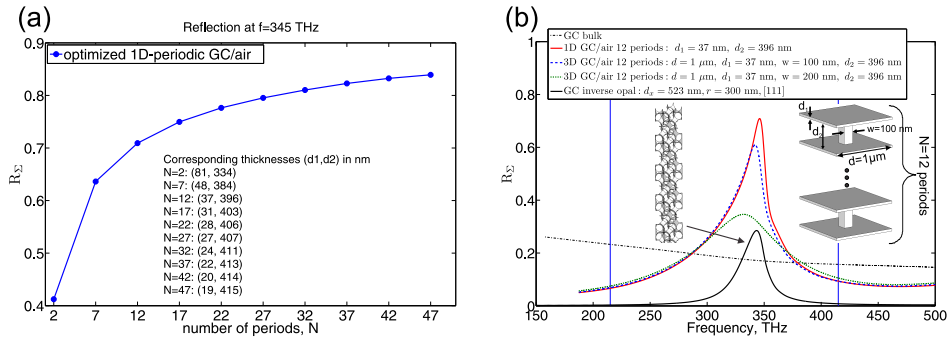

Fig. 4. (a) 1D-periodic GC/air structure optimized for reflection at 345 THz. Two parameters d_1 and d_2 (GC and air thicknesses respectively) were optimized with ES (b) red solid curve - reflectivity of the optimal GC/air structure containing N=12 periods; blue dashed and green dotted curves - reflectivity of 3D GC/air structure (shown in the right inset), with different brick dimensions, w = 100 nm and w = 200 nm respectively; black solid curve - reflection of the inverse opal with the optimal period d_x and sphere radii r.

Evidently, the 1D GC/air structure is not feasible for fabrication. One possible practical realization close to such a 1D periodic structure is shown in Fig. 4(b), where the air layers are substituted with GC bricks, arranged on a square lattice of period $d = 1\ \mu$m. If the ratio $w/d << 1$, the reflectivity of such a 3D structure is close to 1D.

On the other hand, GC inverse opals have been fabricated on the scale of optical wavelengths [15]. We investigated the possibility of such structures to reflect radiation at the aforementioned frequency f=345 THz. The unit cell of an inverse opal, formed by the fcc arrangement of etched spheres and cut in the [111] direction is shown in Fig. 5(a). In the standard configuration $d_x = 2r$, where r is the radius of the spheres and d_x is the period. The connecting bonds in the structure disappear, if $d_x < 1.73r$. Figure 5(b) represents reflectivity of GC inverse opal as a function of r and d_x in the range $1.73r < d_x < 2r$, where the structure is supposed to be feasible for fabrication. The structure taken in calculations contains 36 layers of spheres, this insures that the transmission is below 1%. As can be seen, the optimal parameters are located on the line $d_x = 1.73r$, where the reflectivity reaches $\sim 30\%$. Therefore, the optimal GC inverse opal

[2] There is no mathematical proof for this observation, but it seems reasonable from the physical point of view, since no scattering occurs at planar interfaces.

is extremely sparse. The reflection spectrum of the optimal GC is shown in Fig. 4 by the black solid line. It should be noted that reflectivity drops significantly away from f=345 THz and in fact becomes much lower than bulk GC.

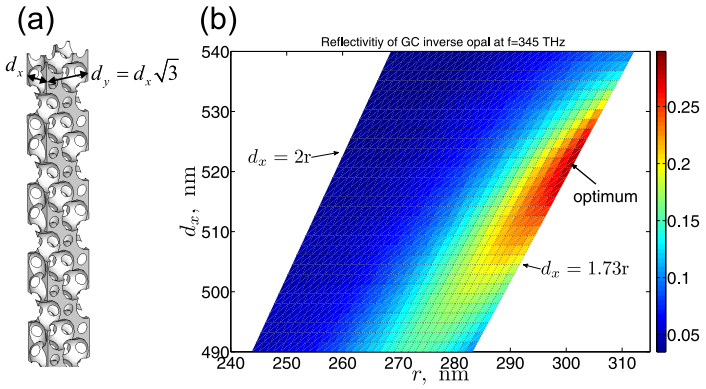

Fig. 5. (a) unit cell of GC inverse opal, formed by the fcc arrangement of spheres (b) reflectivity of GC inverse opal at f=345 THz, as a function of period d_x and sphere radius r.

5. 3D photonic reflectors: silicon carbide guided-mode resonance structures

Resonance reflection with a theoretical efficiency equal to unity can be achieved for transparent periodic dielectric gratings, due to the excitation of leaky modes [16].Experimental realization of high-efficiency guided-mode resonance (GMR) filters was reported in [17, 18]. Energies, linewidths and field distribution of leaky (or quasiguided) modes were calculated in [19].

We explore the idea of GMR for the design of radiation shields for re-entry. The radiation profile u_ν, shown in Fig. 1(a), is strongly nonuniform and contains a number of peaks. The GMR structure can be designed in such a way that the reflection resonances are adjusted to match the radiation peaks. The period of the structure and its height determines the number of excited leaky modes. The geometry of the periodic grating has a strong impact on the excitation efficiency. It appears that even with a relatively simple design a good reflection can be achieved.

Glassy carbon, due to its high absorption, can not utilize the idea of GMR. Therefore, only silicon carbide is considered for GMR structures. We optimized two structures, which are shown in Fig. 6(a) and Fig. 7(a) with the ES algorithm. The only difference between the two structures is that the materials are interchanged air$\leftrightarrow$SiC in the grating region with the thickness l_2. The number of the optimized geometric parameters is four for both structures. Figure 6(b) and Figure 7(b) show the total reflection of the obtained optimal structures. Reflectivity values of the first and second structure are $\langle R_{u_\nu}\rangle \simeq 85\%$ and $\langle R_{u_\nu}\rangle \simeq 83\%$, respectively. The spectral shape of the two GMR structures is quite different. Hereafter, for all of the structures, we also calculate $\langle R\rangle$ for uniformly distributed radiation $u_\nu = 1$. Comparison of $\langle R_{u_\nu}\rangle$ and $\langle R\rangle$ values explicitly shows the correlation of reflection spectra with u_ν. As seen, this correlation is slightly stronger for the second GMR structure.

6. 3D photonic reflectors: silicon carbide woodpile and porous-reflector

SILICON CARBIDE WOODPILE

In this section we consider two other kinds of SiC structures as possible radiation shields for re-entry. Periodic woodpiles were widely studied both theoretically and experimentally. Owing

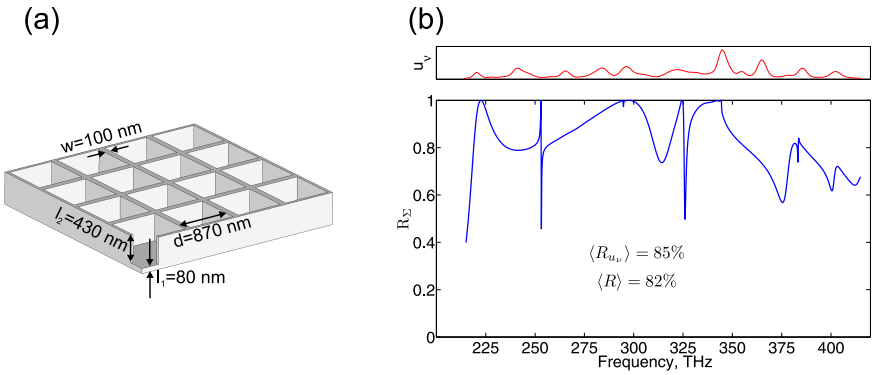

Fig. 6. (a) Silicon carbide GMR structure, optimized for reflection of external radiation u_ν. Ambient material is air. Four parameters, marked with arrows were optimized with ES (b) reflection spectrum of the obtained optimal structure. The radiative spectrum u_ν is depicted above to show the correlation with R_Σ.

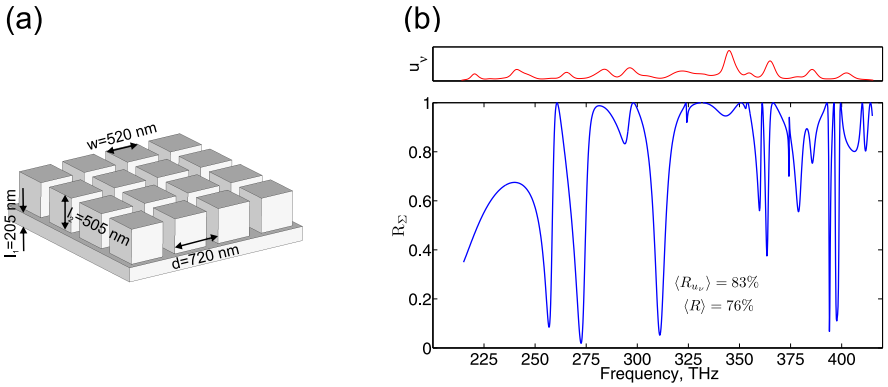

Fig. 7. (a) Silicon carbide GMR structure, optimized for reflection of external radiation u_ν. Ambient material is air. Four parameters, marked with arrows were optimized with ES (b) reflection spectrum of the obtained optimal structure. The radiative spectrum u_ν is depicted above to show the correlation with R_Σ.

to their photonic band gap (PBG), a woodpile can give rise to high reflectivity in the PBG region. However, the PBG of a 3D-periodic SiC woodpile is much narrower than the **B** range. Therefore, a woodpile with a finite number of layers is the object of optimization.

We consider the woodpile as shown in Fig. 8(a). Geometry is determined by the radii of the rods r_i, the angle α at which the rods are arranged with respect to each other and the period d of the square unit cell. The optimal 4- and 8-layered woodpiles, obtained with the ES optimizer are presented in Table 1. Already a 4-layered woodpile demonstrates high reflectivity $\langle R_{u_\nu} \rangle \simeq 91\%$ (see solid green curve in Fig. 8(b)). Increasing the number of layers up to eight, does not give a substantial benefit. The reflectivity is increased only by 2% (see dashed blue curve in Fig. 8(b)). Moreover, many peaks and dips appear in the upper frequency range, above 300 THz. These peaks result from the excitation of leaky modes, that were discussed in Section 5. The number of reflection peaks increases with the increase of the woodpile thickness. This can be explained by means of the empty lattice approximation. In the empty lattice approximation, the woodpile structure is substituted by a homogeneous slab of the same thickness with the averaged permittivity $\langle \varepsilon \rangle$. The waveguide modes of this slab are then folded into the 1st Brillouin zone,

specified by the period of the woodpile d. The resulting dispersion diagrams are shown in Fig. 9. For the 4-layered woodpile, five degenerate resonances are located between 300 – 415 THz (3 s- and 2 p-degenerate modes). For an 8-layered woodpile, eight degenerate resonances (4 s- and 4 p-degenerate modes) are located in the same range. This qualitatively explains, why the spectrum of a thicker woodpile contains more reflection peaks between 300-415 THz.

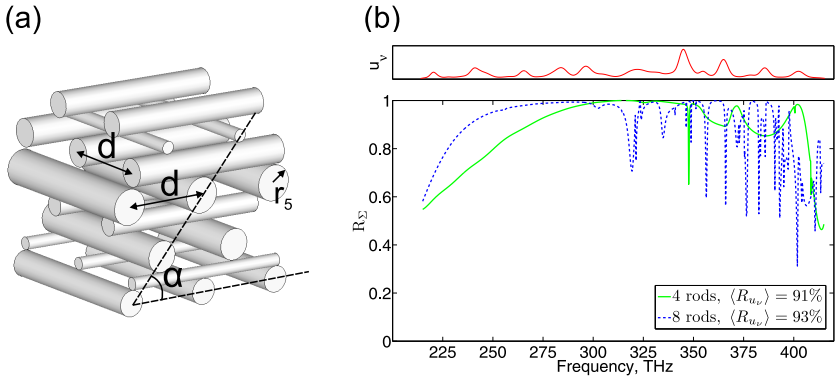

Fig. 8. (a) 8-layered SiC woodpile structure (b) reflection spectrum of woodpile optimized for external radiation u_V. Dips between 300-415 THz are the result of the excitation of the leaky modes.

Table 1. Optimal parameters of woodpile obtained with the ES optimizer for reflectivity in **B**=215-415 THz and sensitivity of the structures to geometrical imperfections

Parameter value, nm										Fitness,%		Sens.,%	
d	α	r_1	r_2	r_3	r_4	r_5	r_6	r_7	r_8	$\langle R_{u_V} \rangle$	$\langle R \rangle$	$\bar{\delta}$	$\delta_{\max}$
654	42°	116	83	87	113	…	…	…	…	91	88	6	16.5
629	40°	96	46	115	75	131	103	47	93	93	90	3	8

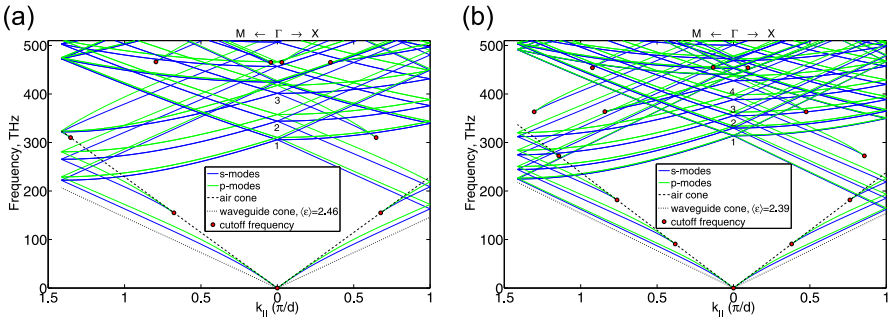

Fig. 9. Dispersion diagrams of the waveguide modes (of the woodpiles, presented in Table 1) in the empty lattice approximation (a) 4-layered woodpile, slab thickness 0.8 μm, $\langle \varepsilon \rangle = 2.46$ (b) 8-layered woodpile, slab thickness 1.4 μm, $\langle \varepsilon \rangle = 2.39$. Resonances in the Γ point between 215-415 THz are marked with numbers.

The final structure considered is shown in Fig. 10 which we call a "porous-reflector". Morphologically this structure is similar to an inverse opal [15], which can be considered as a special type of porous structure.

In inverse opals, the etched spheres are densely packed in either fcc or hcp lattices. In porous-reflectors, in contrast to inverse opals, layers of the etched spheres are separated by a homogeneous layer l_i. The centers of the five etched spheres are located in the center and corners of the rectangular unit cell $(d_x, d_x\sqrt{3})$. The connecting necks between the spheres disappear, if $\xi = d_x/r < 1.73$. We restrict this value to $\xi \geq 1.78$, so that the bonds are not too fragile.

Standard inverse opals do not show a high reflection $\langle R_{u_v} \rangle$, because of the narrow PBG. Reflection spectra of an 8-layered fcc inverse opal, cut in the [111] direction is shown by the black dashed line in Fig.10. In principle, the spectra can be broadened by changing the radii of the spheres in each layer. This, however, can be difficult for fabrication.

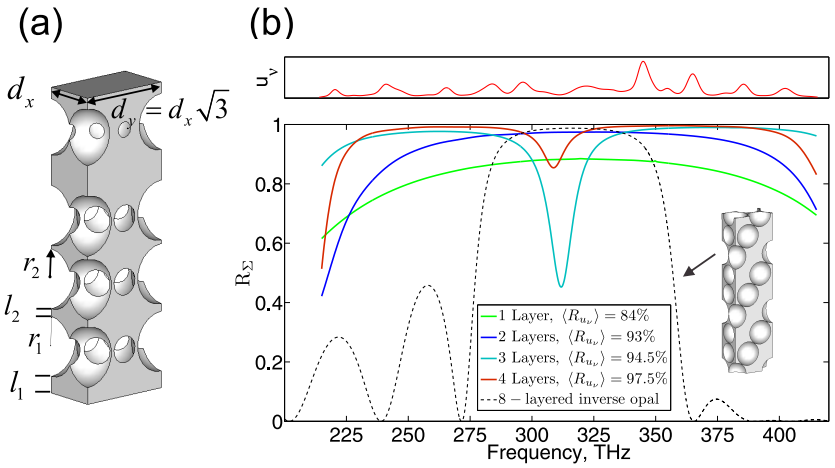

Fig. 10. (a) SiC porous-reflector. Etched spheres are located in the center and corners of a rectangular unit cell (b) reflection spectrum of the porous-reflector with different number of porous layers, optimized for external radiation u_V. Parameters are listed in Table 2. Black dashed curve - spectra of an inverse opal with $r = d_x/2 = 190$ nm, center of PBG coincides with the central frequency $f = 315$ THz.

Table 2. Optimal parameters of a porous-reflector obtained with the ES optimizer for reflectivity in **B**=215-415 THz and sensitivity of the structures to geometrical imperfections

Parameter value, nm										Fitness,%		Sens.,%	
d_x	r_1	l_1	l_2	r_2	l_3	r_3	l_4	r_4	l_5	$\langle R_{u_v} \rangle$	$\langle R \rangle$	$\bar{\delta}$	$\delta_{\max}$
226	127	65	61	…	…	…	…	…	…	84	82	4	16
229	129	59	34	128	61	…	…	…	…	93	91	6	20
230	129	46	136	129	30	129	62	…	…	94.5	93.5	5	15
239	134	74	33	134	15	134	135	125	50	97.5	96	5	15

As in the previous examples, we performed an ES optimization of a porous-reflector for reflection in the **B** range. The optimal parameters are presented in Table 2.

As the number of porous layers increases, the reflection $\langle R_{u_v} \rangle$ approaches unity quite quickly. The spectra of the optimal porous-reflector structures are shown in Fig. 10(b). The small period of the unit cell ensures that the leaky modes are located well above the **B** range. Therefore, the line shape is rather smooth and no sharp reflection peaks/dips are present.

7. Influence of imperfections on reflecting performance

In this section we analyze the influence of geometrical imperfections on the reflecting performance of the considered structures. This analysis is useful for estimating the impact of fabrication inaccuracy on reflection. For simplicity, only those parameters that were optimized by ES are included in the study. Other types of structural imperfections, like roughness [5] and aperiodicity are not considered, even though their impact might be important as well.

The influence of imperfections is studied in a statistical way. For each of the considered structures, $M = 100$ calculations of $\langle R_{u_v} \rangle$ are made. In each calculation all of the geometrical parameters are varied randomly and independently near the optimal value:

$$\mathrm{Par} = \mathrm{Par}^{\mathrm{opt}}(2\eta\zeta - \eta + 1), \tag{5}$$

where $0 \leq \zeta \leq 1$ is a random number and η is the imperfection strength, which is taken $\eta = 0.1$ for all structures. The value δ_{i} represents the decrease of reflectivity $\langle R_{u_v} \rangle$ for the ith calculation:

$$\delta_{\mathrm{i}} = \langle R_{u_v} \rangle - \langle R_{u_v} \rangle_{\mathrm{i}},\ \mathrm{i} = 1, \ldots, M \tag{6}$$

The average decrease of reflectivity out of M calculations is thus:

$$\overline{\delta} = \frac{\sum \delta_{\mathrm{i}}}{M} = \langle R_{u_v} \rangle - \frac{\sum \langle R_{u_v} \rangle_{\mathrm{i}}}{M}, \tag{7}$$

and the value $\delta_{\max}$ represents the maximum decrease of $\langle R_{u_v} \rangle$ in the same set of calculations:

$$\delta_{\max} = \max\left[\delta_1,\ \delta_2,\ \ldots,\ \delta_M\right]. \tag{8}$$

In other words $\overline{\delta}$ and $\delta_{\max}$ determine the average and maximum sensitivity of the structure to imperfections.

The GMR structures studied in Sec. 5 appear to be the most sensitive to geometrical imperfections. For the first GMR structure $\overline{\delta} = 14\%$ and $\delta_{\max} = 31\%$, for the second $\overline{\delta} = 12\%$ and $\delta_{\max} = 29\%$. This implies that fabrication imperfections will strongly degrade the performance of the GMR structures.

The values of $\delta_{\max}$ and $\overline{\delta}$ for the woodpile structure are presented in Table 1. The 8-layered woodpile, while exceeding in reflection a 4-layered only by 2%, is much less sensitive to imperfections, i.e. additional layers help reduce the sensitivity rather than increase reflectivity.

For the porous-reflector $\delta_{\max}$ and $\overline{\delta}$ values are given in Table 2. The average drop of reflectivity is quite low $\overline{\delta} = 4 - 6\%$, while the maximum drop is quite high $\delta_{\max} = 15 - 20\%$.

One-dimensional structures are the least sensitive to disorder. Maximum and average sensitivity for SiC/air structure (shown in Fig. 3(a)) are $\overline{\delta} = 0.5\%$, $\delta_{\max} = 4\%$ respectively. For GC/air structure (shown in Fig. 3(b)) these values are $\overline{\delta} = 0.8\%$, $\delta_{\max} = 3\%$. Practical realizations of a reflector as a one-dimensional structure gives not only high performance, but also good robustness.

The obtained result that reflectivity of 1D structures is the least sensitive to disorder, confirms the statement that 1D structure has the widest band gap for a fixed direction of the wave vector

$\vec{k}$. In Ref. [20] it was shown that in an imperfect photonic crystal of thickness d, in the gap region the transmission is proportional to:

$$T \sim \exp(-4\Delta/Sd(1-\beta\overline{\delta V}^2)), \tag{9}$$

where S is the speed of light in the appropriate band, Δ is the gap value, $\beta \sim 1$ is a numerical parameter, and $\overline{\delta V}$ is the average deviation of the specific volume from the ideal structure. Therefore, among the structures with the same fixed disorder $\overline{\delta V}$, the ones with larger Δ will transmit less light, or accordingly reflect more.

8. Conclusion

Different types of photonic structures composed of glassy carbon and silicon carbide were analyzed, as potential radiation shields for atmospheric re-entry. S-matrix and CST Studio (Frequency Domain Solver) were used as field solvers and evolutionary strategy was used as an optimizer. Structures were optimized for the near-infrared part of the radiative spectra profile. Reflectivity of GC structures, in contrast to SiC, are significantly limited, due to material absorption.

Silicon carbide, being optically transparent in the near-infrared, allows us to design highly reflecting structures in a number of different ways. We optimized one-dimensional structures, woodpiles, guided-mode resonance structures and porous-reflectors.

Sensitivity analysis of the obtained optimal structures was performed, in order to estimate the role of fabrication tolerances on reflectivity.

GMR structures are expected to be the most sensitive to fabrication inaccuracies. Woodpiles and porous reflector are much less sensitive. One-dimensional structures are expected to be the most robust to geometrical imperfections and therefore, are of greatest interest for re-entry applications.

Acknowledgements

The authors are grateful to the colleagues from NASA Ames Research Center, namely to Brett Cruden and Dinesh Prabhu for discussions and to Aaron Brandis for providing the experimental data of radiative spectra, obtained in the NASA Ames Research Center's EAST facility.